Sensitivity of Water Balance in the Qaidam Basin to the Mid-Pliocene Climate

Xun Wang[1,*], Benjamin Schmidt[1*], Marco Otto[1], Todd A. Ehlers[2], Sebastian G. Mutz[2], Svetlana Botsyun[2], Dieter Scherer[1]

[1]Chair of Climatology, Technische Universitt Berlin, Berlin, Germany
[2]Department of Geosciences, University Tbingen, Tbingen, Germany

Key Points:

- ECHAM5 global climate simulations for present day and the mid-Pliocene were dynamically downscaled
- Downscaling results show a higher water balance in the Qaidam Basin under mid-Pliocene climate conditions
- The higher water balance in the Qaidam Basin under mid-Pliocene conditions is closely associated with changes in the mid-latitude westerlies and in the East Asia Summer Monsoon

*X. Wang and B. Schmidt should be considered joint first author

Corresponding author: Xun Wang, xun.wang@tu-berlin.de

Corresponding author: Benjamin Schmidt, benjamin.schmidt@tu-berlin.de

Abstract

The Qaidam Basin (QB) in the northeastern Tibetan Plateau held a mega-lake system during the Pliocene. Today, the lower elevations in the basin are hyperarid. To understand the mechanisms behind this system change, we applied the Weather Research and Forecasting model for dynamical downscaling of ECHAM5 global climate simulations for present-day (PD) and mid-Pliocene (PLIO) conditions. In PLIO, the annual water balance (ΔS) of the QB is higher than that in PD, resulting from a stronger moisture influx across the western border in winter, spring, and autumn and a weaker moisture outflux across the eastern border in summer. The atmospheric water transport across both borders is influenced by the mid-latitude westerlies throughout the year. The jet stream over the QB is stronger in PLIO in winter, spring, and autumn, causing stronger moisture input at the basin's western border in these seasons. In summer, the jet strength over the QB decreases in PLIO. Meanwhile, the East Asian Summer Monsoon (EASM) intensifies and migrates to the Northwest, transporting moisture into the QB. Thus, the weaker moisture output through the eastern border in summer is a combined result of weakened jet strength and the strengthening of the EASM. Therefore, the differences in ΔS between PLIO and PD are coupled with changes in the mid-latitude westerlies and the EASM. Given that the mid-Pliocene climate is an analog of the projected warm climate of the near future, our study contributes to a better understanding of the impacts of climate change in Central Asia.

1 Introduction

The Qaidam Basin (QB) is an intermontane endorheic drainage basin located in the northeastern Tibetan Plateau (TP) (Figure 1). The central and lower elevation part of the QB is hyperarid today, but paleogeographic studies revealed that the QB contained a freshwater mega-lake system during the Pliocene (Kezao & Bowler, 1986; Mischke et al., 2010; J. Wang et al., 2012) even though the basin and surrounding mountain areas experienced a general aridification throughout the Pliocene (Rieser et al., 2009; Y. F. Miao et al., 2013). With the beginning of the Pleistocene, the mega-lake system began to shrink. This process continued over the course of the Pleistocene until today when only a few playas and saline lakes remain (J. Wang et al., 2012).

In the mid-Pliocene ($\sim$3 Ma), the global climate was warmer and the CO_2 concentration in the atmosphere was higher than today, but the paleogeographic features were similar to those of today (Dowsett et al., 2010). The existence and the stable state of the mega-lake system during this period indicate that the long-term water balance (ΔS) of the QB must have been non-negative. ΔS is the total change in water storage within all the reservoirs inside the drainage basin. For an endorheic drainage basin like the QB, ΔS can be expressed as the spatial average of net precipitation ($P-ET$), i.e., the difference between precipitation (P) and evapotranspiration (ET), over the total area of the basin (Scherer, 2020). Thus, to answer how the lake system could survive the continuous aridification and maintain its stability throughout the Pliocene, first of all, it is important to understand how ΔS in the QB responds to different climate conditions and what are the mechanisms behind the changes of ΔS in the QB. Central Asia is home to nearly half of the arid areas on Earth. Lakes serve as an important water resource in central Asia but exhibit sensitivity and vulnerability to climate change (Yapiyev et al., 2017). The mid-Pliocene climate is considered as an analog of near-future climate (Burke et al., 2018). Thus, investigating the changes of ΔS under the mid-Pliocene climate can help us understand the lake development in the future and contribute to water resource management in central Asia.

A recent study by Scherer (2020) revealed that under the present climate conditions, the ΔS in the QB is close to zero and the specific humidity, in combination with the air temperature, is the climate driver of annual ΔS in the QB. A slight increase in specific humidity could result in a significant increase in mean annual ΔS. Thus, under the wetter and warmer climate conditions of the mid-Pliocene, annual ΔS in the QB could have been

positive, so the Qaidam mega-lake system could have been sustained. However, the large-scale controlling mechanisms of the ΔS in the QB are still unknown. On the climatological scale, ΔS and net moisture transport into and out of an endorheic basin through its lateral boundary are in balance (Brubaker et al., 1993). Therefore, the changes of ΔS in the QB are linked to the changes in atmospheric water transport (AWT).

The goal of this study is to answer the following research questions:

1) How does ΔS of the QB change under the mid-Pliocene climate condition?
2) How does the AWT over the QB differ from the mid-Pliocene climate to the present-day climate?
3) Which large-scale systems regulate the changes in AWT and ΔS in the QB?

In this study, we employed the Weather Research and Forecasting model (WRF) as the Regional Climate Model (RCM) to dynamically downscale ECHAM5 global climate simulations to 30 km grid spacing. Two sensitivity experiments were conducted, which were driven by the present-day and mid-Pliocene global climate simulations, respectively. The output of WRF can provide a physically consistent picture of present-day and mid-Pliocene climate. Additionally, compared to the forcing data from the global model, the high-resolution WRF output represents the topography in more detail and can better resolve fundamental processes over complex terrains, such as orographicallyinduced precipitation. Note that the intention of this study is not to reconstruct the regional climate in the QB during the mid-Pliocene. Here, we simulated the regional climate of the QB and its surrounding areas with modern geographic conditions. This means only the required meteorological fields from the ECHAM5 model were applied to drive the WRF model. In this way, we can analyze the large-scale controls of ΔS in the QB independently from e.g., land cover controls.

The paper is organized as follows: we describe the methods used in this study in the following section. Section 3 presents the dynamical downscaling results for differences in ΔS (section 3.1), AWT (section 3.2), and large-scale circulation patterns (section 3.3) between the mid-Pliocene and the present climate. We discuss our results, compare them to other studies in Section 4. Conclusions are drawn in section 5.

2 Data and Methods

2.1 Global climate simulations

For the global climate simulations, we used isotope tracking ECHAM5-wiso atmospheric general circulation model (AGCM), which is developed at Alfred Wegener Institute and based on the ECHAM5 model of the Max Planck Institute for Meteorology, Hamburg (Roeckner et al., 2003). The model is well-established and included in the Coupled Model Intercomparison Projects (CMIPs) (Meehl et al., 2007; Taylor et al., 2012). The ability of ECHAM5-wiso to reproduce modern and paleoclimates on both global and regional scales has been shown in multiple studies (Mutz et al., 2016, 2018; Botsyun et al., 2020).

We performed ECHAM5-wiso simulations at a T159 spectral resolution (equivalent to a grid spacing of $\sim$0.75°) with a vertical resolution of L31 (31 levels up to 10 hPa). The control simulation (PD_GCM) used present-day boundary conditions including the AMIP2 sea surface temperature and sea ice data from 1957 to 2014 and observed greenhouse gas concentrations for the same period (Nakicenovic et al., 1990). The simulation was conducted for more than 40 model years. A climatological reference period of 15 years was established for the analysis presented here using the simulation years 20002014 to represent the most recent climate conditions. We also performed a paleoclimate experiment, representing the climate conditions of the mid-Pliocene (PLIO_GCM, $\sim$3 Ma). The setups and boundary conditions of PLIO_GCM for ECHAM5 are identical to those of Mutz et al. (2018) and Botsyun et al. (2020). In PLIO_GCM, we accounted for changing pCO2, land

surface conditions including vegetation change and land ice, albedo, orbital variation, and sea-surface temperatures, which potentially cause changes in the hydrological cycle. The PLIO_GCM experiment was conducted for 18 years, including 3 years necessary for model spin-up. Both PD_GCM and PLIO_GCM experiments were validated against observed and modeled climate patterns (Mutz et al., 2018; Botsyun et al., 2020).

2.2 Dynamical Downscaling

We employed WRF version 4.1.2 as the RCM for the dynamical downscaling of GCM data. Two sensitivity experiments were conducted using 15-year time slices from PD_GCM and PLIO_GCM simulated by ECHAM5 (section 2.1) as initial and boundary conditions. These two WRF experiments are referred to as PD and PLIO in the following text. Except for the atmospheric forcing data, other parameters were kept the same in both experiments (Table 1).

We set the model domains (Figure 1) grid spacing to 30 km. In the vertical direction, 28 terrain-following eta-levels were used. The model time steps are 120 seconds with a 6 hourly data output. The boundary conditions were updated every 6 h. We employed the daily re-initialization strategy from Maussion et al. (2011, 2014), where we initialize a model run for every 24 h period. Each simulation starts at 12 UTC and contains 36 h, with the first 12 h as the spin-up time. This strategy kept the large scale circulation patterns simulated by WRF closely constrained by the forcing data, while concurrently allowing WRF to develop the mesoscale atmospheric features. Physical parameterization schemes were consistent with the ones used for high-resolution dynamical downscaling in High Mountain Asia in X. Wang et al. (2020).

To examine the ability of the model to reproduce the present-day climate patterns, PD predicted climate is compared with ERA5 reanalysis data of the European Centre for Medium-Range Weather Forecasts (Copernicus Climate Change Service (C3S), 2017) with regard to P and AWT (Figure S1). PD generally reproduces the spatial patterns of P and AWT. But there exist some discrepancies in the amount of P and AWT.

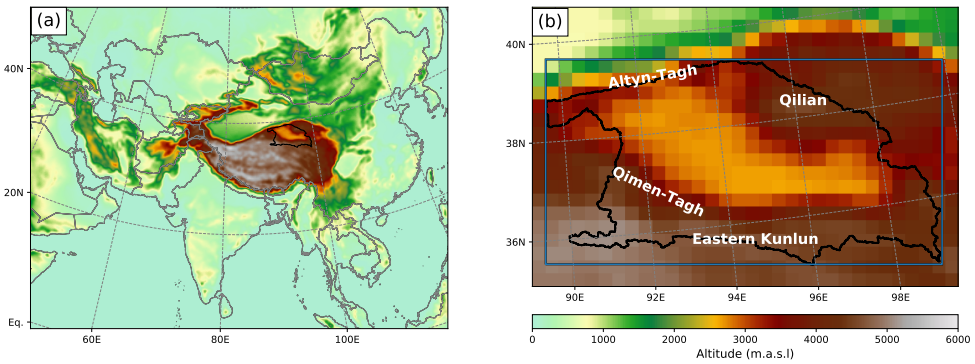

Figure 1. (a) Map of WRF model domain; (b) overview of the Qaidam Basin. Black line: boundary of the Qaidam Basin (Lehner & Grill, 2013). Blue rectangle: Qaidam box for atmospheric moisture budget analysis.

2.3 Data analysis

According to Scherer (2020), for large endorheic drainage basins like the QB, surface runoff is zero by definition, while groundwater runoff can be neglected. Thus, ΔS of the

Table 1. WRF Model configuration.

Maps and grids	
Map projection	Lambert conformal conic
Horizontal grid spacing	30 km (281 x 217 grid points)
Vertical levels	28 Eta-level
Forcing strategy	
Forcing data	ECHAM5 time slices PD_GCM and PLIO_GCM
Lake surface temperature	Substituted by daily mean surface air temperature
Initialization	Daily
Runs starting time	Daily at 12:00 UTC
Runs duration	36 h
Spin-up time	12 h
Physical parameterization schemes	
Longwave radiation	RRTM scheme (Mlawer et al., 1997)
Shortwave radiation	Dudhia scheme (Dudhia, 1989)
Cumulus	Kain-Fritsch cumulus potential scheme (Berg et al., 2012)
Microphysics	Morrison 2-moment scheme (Morrison et al., 2009)
Planetary boundary layer	Yonsei University scheme (Hong et al., 2006)
Land surface model	Unified Noah land surface model (Tewari et al., 2004)
Surface layer	revised MM5 surface layer scheme (Jiménez et al., 2012)

QB can be expressed as the spatial average of $P - ET$ over the total area of the QB:

$$\Delta S =< P - ET > \tag{1}$$

Angle brackets indicate a spatial average over the whole area of the QB (black line in Figure 1b).

Following Curio et al. (2015), AWT is calculated as the vertical integration of water flux over the whole atmospheric column along the model eta-levels from the surface (z_{sfc}) to top (z_{top}):

$$Q = \int_{z=z_{sfc}}^{z_{top}} v_h \rho q \Delta z \tag{2}$$

where v_h is the horizontal wind vector ($\mathrm{m\,s^{-1}}$), ρ is the dry air density ($\mathrm{kg\,m^{-3}}$), q is the specific humidity ($\mathrm{kg\,kg^{-1}}$) for all water species, which is converted from the mixing ratio of water vapor, liquid water, and solid water; Δz is the thickness of each eta-level (m), which is not constant but changes over time and increases with height.

The shape of the QB is very irregular (black line in Figure 1b). A simple rectangle covering the QB (hereafter referred to as Qaidam box) was defined to perform budget analysis on the AWT across the four borders (blue rectangle in Figure 1). This method is widely used to estimate the moisture input and output within a certain area (e.g., Feng & Zhou, 2012; Koffi et al., 2013; Z. Wang et al., 2017). The AWT at each border was calculated and converted to the theoretical precipitation amount. The atmospheric moisture budget of the Qaidam Box was then calculated as the sum of the AWT at all borders.

We applied two-sample t-tests to find significant differences between PD and PLIO. The interpretation of a large number of local hypothesis tests requires stricter significance threshold values for every local test, to ensure the global null hypothesis can be rejected

with a certain global significance level. Thus, for spatial representation, we applied the false discovery rate (FDR) approach proposed by Wilks (2016), which aims to control the FDR, i.e. the rate at which local null hypotheses are falsely rejected. We sorted the p-values of the local tests in ascending order and defined new thresholds according to equation 3 taken from Wilks (2016):

$$p^*_{FDR} = \max_{i=1,\ldots,N}[p_i : p_i \leq (i/N)\alpha_{FDR}] \tag{3}$$

with p^*_{FDR} as the modified threshold value for rejecting a local null hypothesis, p_i as the p-value of a local test, and α_{FDR} as the chosen control level for the FDR. Employing equation 3, we reduced the FDR choosing a control level of $\alpha_{FDR} = 0.05$ and adjusted local threshold values accordingly. This yields a global significance level of $\alpha \leq 0.05$ depending on spatial autocorrelation in the data.

3 Results

3.1 Comparison of ΔS and its components

In this section, we focus on the changes in ΔS and its components in the High Mountain Asia region and the QB. Figure 2-4 show the downscaling results for P, ET, and $P - ET$ for PLIO and PD and the difference between the two. In Table 1, we present seasonal and annual values of P, ET, ΔS, air temperature at 2 m ($T2$) and specific humidity at 2 m ($Q2$) averaged over the QB (black line in Figure 1). We define seasons as commonly done in meteorology, spanning three months each: winter (December-February, DJF), spring (March-May, MAM), summer (June-August, JJA), and autumn (September-November, SON).

Over the High Mountain Asia region, simulated P is enhanced in PLIO over the Himalayas, the northern TP, the Tarim Basin, and the Tien Shan. Lower P in PLIO can be found in the central TP and Pamir-Karakoram (Figure 2c). In the QB, P strongly correlates with the altitude for both simulations, due to orographically-induced precipitation (Figure 2a, 2b). PLIO generally has higher values of P in the QB, and the largest difference can be found in the Qilian Mountains, the Altyn-Tagh Mountains, and the Qimen-Tagh ranges. However, the difference is not significant in the Eastern Kunlun Mountains, which is located in the transition area of positive and negative values of P difference between PLIO and PD (Figure 2c). Averaged over the whole QB, we see increased P in all seasons in PLIO with a difference between PLIO and PD of $63\,\mathrm{mm\,a^{-1}}$ (Table 2).

The spatial patterns of the differences in ET between PLIO and PD (Figure 3c) generally follow those of the differences in P (Figure 2c) in the larger part of the domain. In these regions, it is not the availability of energy for latent heat, but water availability that limits ET. We find a different situation in the Pamir-Karakoram region, the northern slopes of the central Himalayas and the south-eastern part of the QB. This opposite change of P and ET in the above-mentioned regions indicates that energy availability must be the limiting factor for ET. In the QB, ET mainly takes place in the mountain areas, where most of the precipitation occurs (Figure 3a, 3b). Averaged over the whole QB, PLIO shows an increase in ET of $36\,\mathrm{mm\,a^{-1}}$ as compared to PD.

For $P - ET$, PLIO and PD yield similar spatial patterns over High Mountain Asia, with negative $P - ET$ over the western TP, the Tarim Basin, and some parts of the QB (Figure 4a, 4b). In PLIO, $P - ET$ is significantly decreased over the central TP, the Tarim Basin, and Pamir-Karakoram. The annual ΔS in the QB as a whole is higher under the mid-Pliocene climate, but the difference is not statistically significant (Table 2). Spatially, higher ΔS in PLIO can be found in the eastern and central parts of the QB (Figure 4c). Seasonally, PLIO has a significantly higher ΔS in the QB in winter, spring, and autumn. In summer, the difference in ΔS between PLIO and PD is negative, though not significant (Table 2).

The global climate in the mid-Pliocene is believed to be warmer and wetter than the modern climate, which is also shown in our ECHAM5 global simulations. However, this is not true for the regional climate signal in the QB. While the local $Q2$ signal averaged over the QB is consistent with the global signal, the local $T2$ in the QB is 2 K lower in PLIO (Table 2).

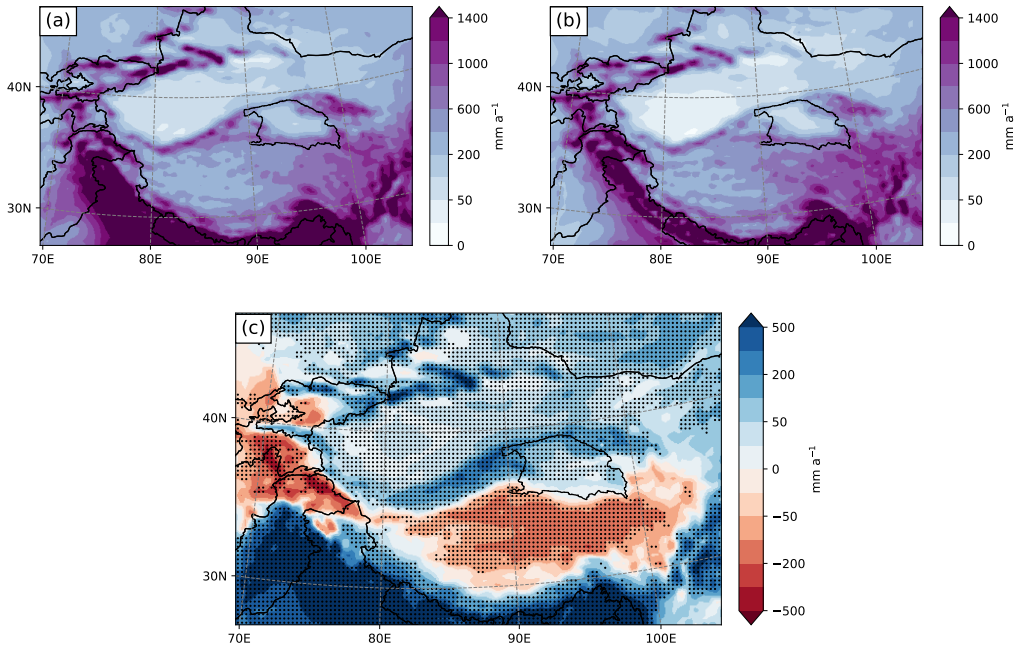

Figure 2. 15-year average of annual precipitation P (mm a^{-1}) for (a) PLIO and (b) PD; (c) difference between PLIO and PD. Dotted regions are significant ($\alpha_{FDR} = 0.05$, $p^*_{FDR} = 0.035$; two-sample t-test).

3.2 Comparison of AWT

Since ΔS is linked to the large-scale AWT, in this section, we compare AWT between PLIO and PD. Table 3 presents the seasonal and annual AWT through each border of the Qaidam box (blue rectangle in Figure 1b), as well as the sum of AWT from all borders, i.e., the atmospheric moisture budget. In both PLIO and PD, the western and eastern border of the Qaidam box serves as the dominant moisture input and output channel, respectively. The higher annual moisture budget in PLIO derives from the increased moisture influx across the western border and the decreased moisture export at the eastern border (Table 3). In PLIO, the increased moisture influx at the western border occurs in winter, spring, and autumn, while the strong and significant reduction of moisture export at the eastern border occurs in summer. This indicates that moisture budget and ΔS in the QB is related to the large-scale systems that influence the AWT at the western and eastern borders.

Figure 5 illustrates the seasonal route and the magnitude of the moisture propagation across the whole domain. In both PD and PLIO, the mid-latitude westerlies control the AWT in the QB throughout the year. In winter, spring and autumn, there exists an eastward moisture transport in the difference plots (Figure 5c, f, l), indicating a stronger moisture transport by the mid-latitude westerlies in PLIO in these seasons. This is supported by higher moisture input at the western border and higher output at the eastern border in

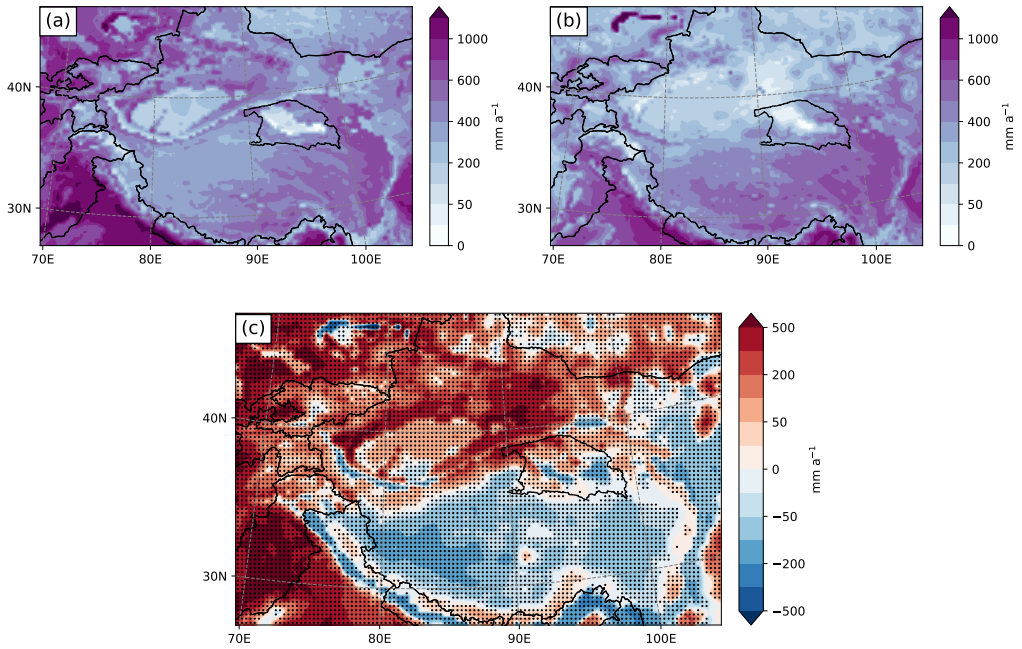

Figure 3. 15-year average of annual evapotranspiration ET ($\mathrm{mm\,a^{-1}}$) for (a) PLIO and (b) PD; (c) difference between PLIO and PD. Dotted regions are significant ($\alpha_{FDR} = 0.05$, $p^*_{FDR} = 0.045$; two-sample t-test).

these seasons. In summer months, the influence of the mid-latitude westerlies is weaker in PLIO, as shown by the anomalous westward moisture transport over the QB in Figure 5i. Accordingly, the moisture input at the western border and the output at the eastern border are significantly lower in PLIO.

In summer months, moisture transport is predominantly from the southwest due to the Indian Summer Monsoon (ISM). This northeastward transport over the TP into the QB through the southern border of the Qaidam box is stronger in PD than that in PLIO (Figure 5g, h, i, Table 3). Additionally, the moisture transport over eastern Asia by the East Asian Summer Monsoon (EASM) is stronger in PLIO. However, from Figure 5 it is unclear whether the EASM also contributes to the water transport into the QB. Analysis of the daily zonal water transport on the eastern border of the Qaidam box shows moisture input from the eastern border into the QB in PLIO from the middle of July to the beginning of August (Figure 6), which indicates the influence of the EASM in PLIO. This pattern can not be observed in PD. The additional moisture input by the EASM in PLIO also contributes to the lower values for total moisture output at the eastern border in summer.

3.3 Comparison of large-scale circulation patterns

The results in section 3.2 show the higher ΔS and moisture budget in PLIO are caused by differences in the AWT at the western and eastern borders of the Qaidam box. In this section, we examine the large scale systems that control the AWT across these two borders.

The AWT at both the western and eastern borders is under the influence of the mid-latitude westerlies throughout the year. The seasonal zonal wind speed along a latitude-pressure transect across the longitudinal range of the QB (89°-100°E) for PLIO and PD

Table 2. Seasonal and annual precipitation P (mm season^{-1} or mm a^{-1}), evapotranspiration ET (mm season^{-1} or mm a^{-1}), water balance ΔS (mm season^{-1} or mm a^{-1}), air temperature at 2 m $T2$ (°C) and specific humidity at 2 m $Q2$ (g kg^{-1}) averaged over the Qaidam Basin for PLIO, PD and the difference between PLIO and PD (PLIO-PD). Significant differences with $\alpha = 0.05$ ($\alpha = 0.01$) are underlined (underlined and bold).

	PLIO					PD					PLIO-PD				
	P	ET	ΔS	T2	Q2	P	ET	ΔS	T2	Q2	P	ET	ΔS	T2	Q2
DJF	51	22	29	-13.9	1.3	43	25	19	-12.2	1.3	8	**-3**	11	**-1.7**	0.0
MAM	131	87	43	-2.7	3.4	111	83	27	0.0	3.1	**20**	4	17	**-2.7**	**0.3**
JJA	163	152	12	8.7	7.4	151	122	29	9.9	6.0	13	**30**	-17	**-1.2**	**1.4**
SON	74	62	12	-3.3	3.3	52	56	-4	-1.0	3.0	**22**	**6**	**16**	**-2.3**	**0.3**
Annual	419	322	96	-2.8	3.9	356	286	70	-0.8	3.4	**63**	**36**	26	**-2.0**	**0.5**

Table 3. 15-year average of seasonal and annual atmospheric water flux converted to theoretical precipitation amount (mm season^{-1} or mm a^{-1}) through each border of the Qaidam box (Blue rectangle in Figure 1b). Positive values indicate moisture input into the Qaidam Basin, while negative values represent moisture output. Significant differences with $\alpha = 0.05$ ($\alpha = 0.01$) are underlined (underlined and bold).

	PLIO					PD					PLIO-PD				
	West	East	South	North	Sum	West	East	South	North	Sum	West	East	South	North	Sum
DJF	327	-298	-38	28	19	277	-248	-7	-2	19	**50**	**-50**	**-31**	**30**	0
MAM	433	-399	50	-49	36	390	-368	19	-14	28	43	-31	31	-35	**8**
JJA	344	-283	120	-174	8	407	-459	159	-95	12	**-63**	**176**	-39	-79	**-4**
SON	315	-414	71	-79	-7	368	-394	95	-80	-11	47	-20	-24	1	4
Annual	1519	-1393	204	-274	56	1441	-1469	267	-191	48	78	76	-63	-83	**8**

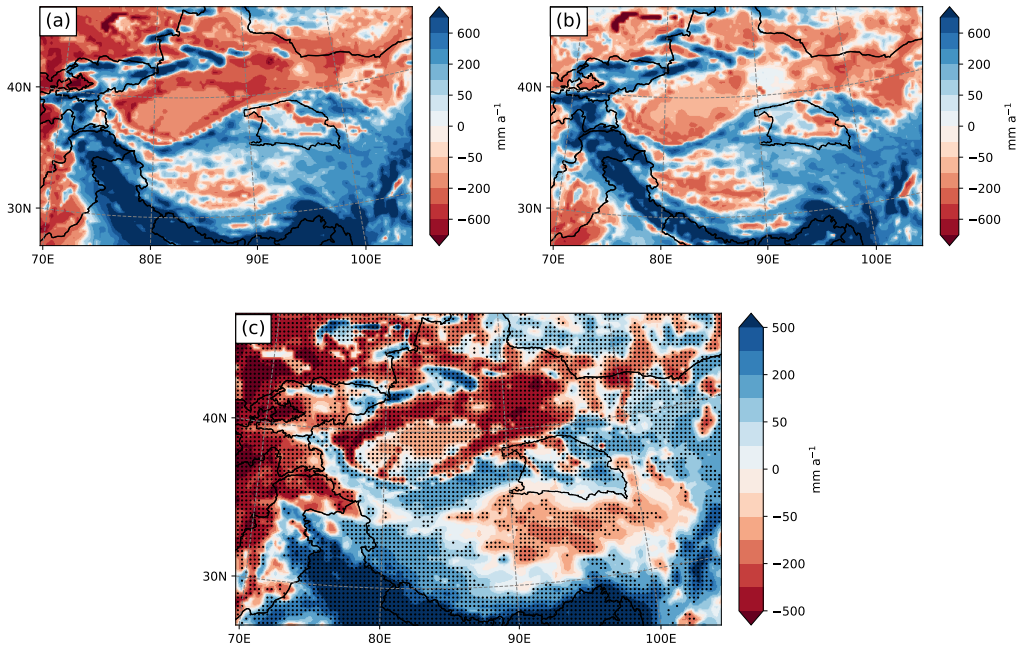

Figure 4. 15-year average of annual net precipitation $P-ET$ (mm a^{-1}) for (a) PLIO and (b) PD; (c) difference between PLIO and PD. Dotted regions are significant ($\alpha_{FDR} = 0.05$, $p^*_{FDR} = 0.033$; two-sample t-test).

is presented in Figure 7. In both PLIO and PD, the mid-latitude westerlies show seasonal migrations: a southward extension from summer to winter and a northward contraction from winter to summer. The maximum zonal wind speed occurs at around 200 hPa in all seasons. PLIO shows a poleward shifted and contracted westerly zone. Following the methods used by J. Sun et al. (2020), we defined a strength index as the average maximum zonal wind speed at 200 hPa at each longitude over the Qaidam box to quantify the strength of the westerlies over the QB. Under the mid-Pliocene conditions, the westerlies over the QB are stronger in all seasons except for summer (Figure 8), which explains the larger AWT through the western and eastern borders (Table 3).

Figure 9 shows the 500 hPa geopotential height and wind field in summer for PLIO and PD. The Northwest Pacific subtropical high (NPSH) intensifies and extends westwards in PLIO, indicated by higher geopotential and stronger anti-cyclonic circulation over eastern China (Figure 9). The NPSH is a major component of the subtropical EASM and regulates the northern edge of the EASM (Huang et al., 2019). The strengthening of the EASM in PLIO is coupled with a tilted jet stream axis over northeastern China. The influence of the EASM on the QB is not visible in the climatology of the summer wind field at the 500 hPa level. Therefore, we selected the period from 17 July to 27 July, when the daily AWT averaged over all the grid points at the eastern border of the Qaidam Box is negative, to define the period, when the QB is under the direct influence of the EASM. The geopotential height and wind field at 500 hPa in this period are presented in Figure 10. During this period, the NPSH intensifies and extends further northwestward in both PLIO and PD, as compared to the climatology in the summer. In PLIO, the southern part of the QB is clearly under the control of easterly winds in this period (Figure 10a).

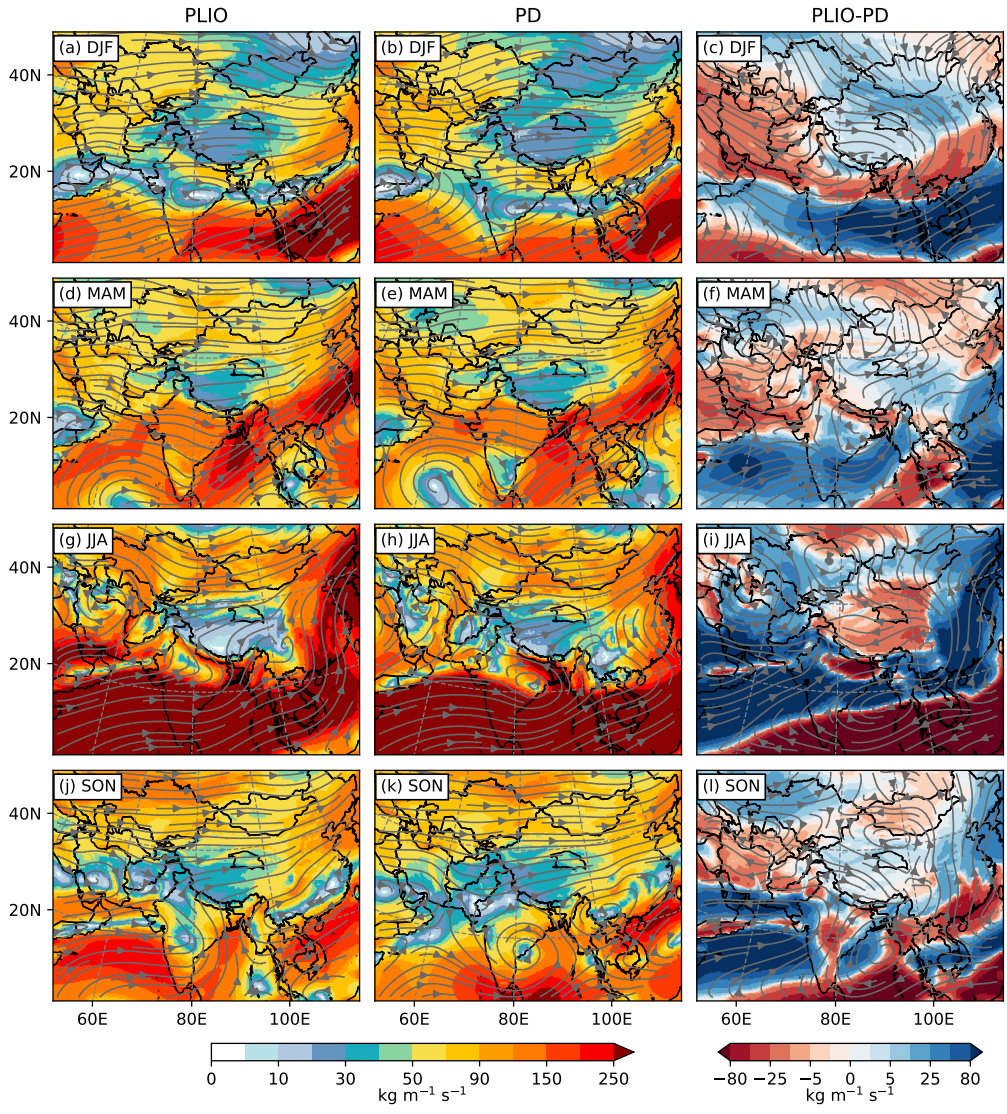

Figure 5. 15-year mean seasonal atmospheric water transport ($\mathrm{kg\,m^{-1}\,s^{-1}}$) in DJF (a, b, c), MAM (d, e, f), JJA (g, h, i) and SON (j, k, l) for PLIO (a, d, g, j), PD (b, e, h, k), and difference between PLIO and PD (c, f, i, j). Colors represent the strength of water vapor flux; arrows indicate transport direction.

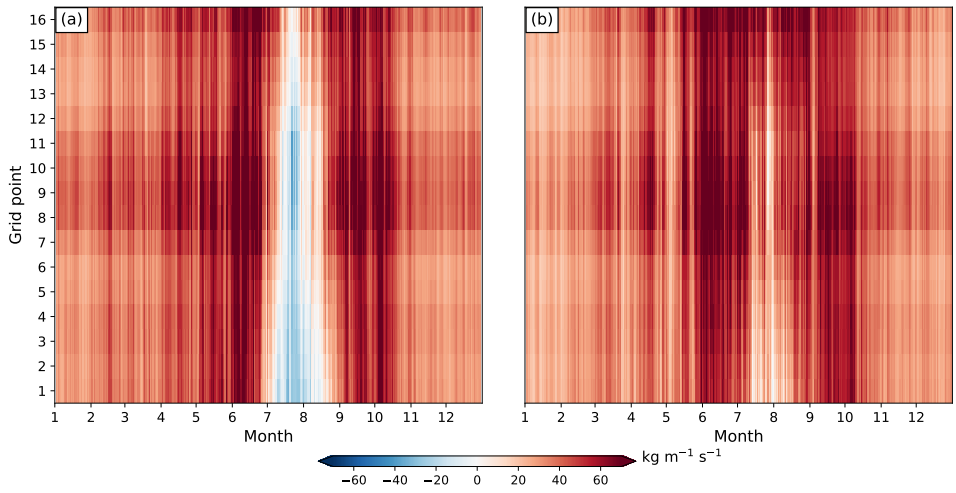

Figure 6. 15-year average of daily zonal atmospheric water transport ($\mathrm{kg\,m^{-1}\,s^{-1}}$) of 16 grid points at the eastern border of the Qaidam box (Blue rectangle in Figure 1b) for (a) PLIO and (b) PD. Grid point 1 and grid point 16 represent the south-most and north-most grid point. Reddish colors indicate water transport away from the Qaidam Basin, while blueish colors indicate water transport towards the Qaidam Basin.

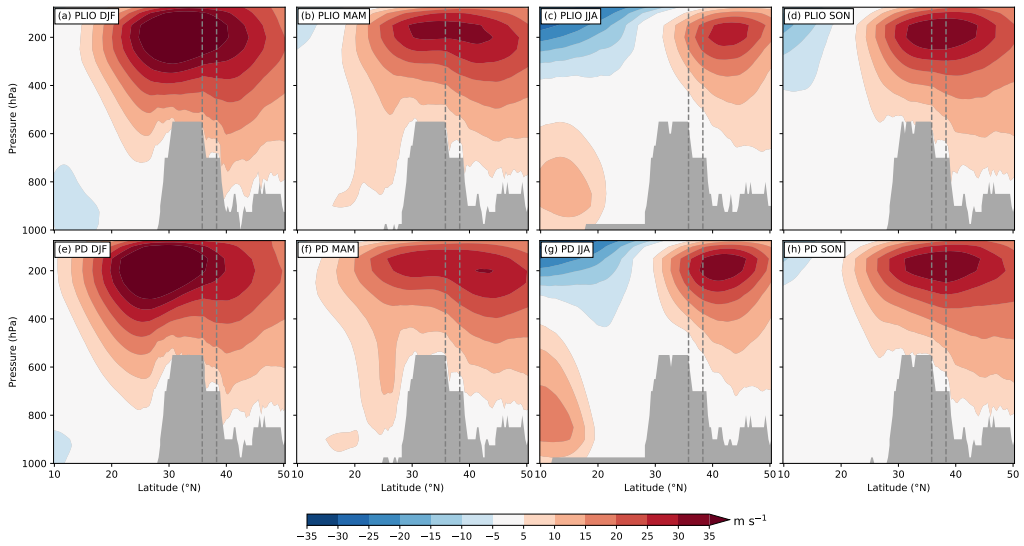

Figure 7. 15-year average of seasonal zonal wind speed ($\mathrm{m\,s^{-1}}$) along a latitude pressure transect averaged from 89°-100°E for PLIO (a, b, c, d) and PD (e, f, g, h) in DJF(a, e), MAM(b, f), JJA(c, g) and SON(d, h). Dashed lines show the latitudinal range of the Qaidam Basin.

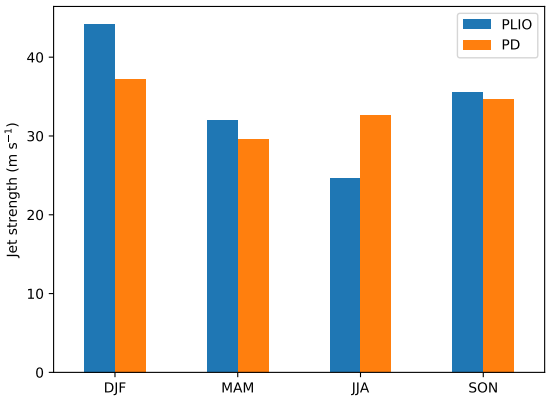

Figure 8. 15-year average of seasonal strength index of jet stream ($\mathrm{m\,s^{-1}}$) over the Qaidam Basin for PLIO and PD, calculated as defined in J. Sun et al. (2020).

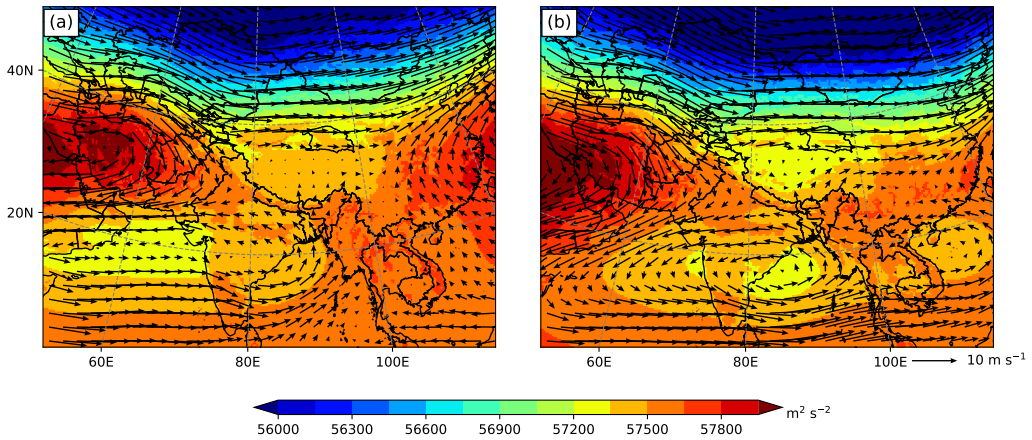

Figure 9. 15-year climatology of geopotential (shading, $\mathrm{m^2\,s^{-2}}$) and wind field (arrows, $\mathrm{m\,s^{-1}}$) at 500 hPa in JJA for (a) PLIO and (b) PD.

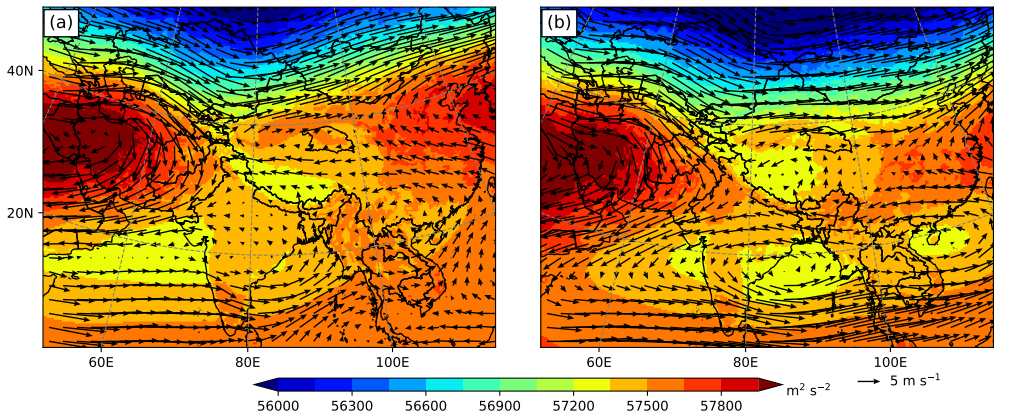

Figure 10. 15-year climatology of geopotential (shading, $\mathrm{m^2\,s^{-2}}$) and wind field (arrows, $\mathrm{m\,s^{-1}}$) at 500 hPa from 17 July to 27 July for (a) PLIO and (b) PD.

4 Discussion

4.1 Implications of the higher ΔS in PLIO

As previously mentioned, the PLIO simulation presented here cannot be considered as a reconstruction of the regional climate in the QB for the mid-Pliocene. We took only required meteorological fields from the ECHAM5 model to drive the WRF model. High-resolution reconstruction of the Pliocene climate at a grid spacing of 30 km would also require Pliocene surface conditions, such as topography, land cover, etc. at an equivalent or even higher resolution, which are not available to date. The most commonly used surface boundary conditions for mid-Pliocene simulations are from the US Geological Surveys Pliocene Research Interpretation and Synoptic Mapping (PRISM) project (Dowsett et al., 1994). The most recently released PRISM4 data set has a $1^\circ \times 1^\circ$ grid spacing (Dowsett et al., 2016), which is too coarse for regional climate simulations. Moreover, the exact extent and location of the Qaidam mega-lake system in the mid-Pliocene is unknown, which further prevents the reconstruction of regional climate using RCM. Thus, we applied the same geographical static data provided by WRF for both PLIO and PD simulations. The PLIO simulations provide a virtual world, which allows us to investigate the response of the regional hydroclimate in the QB with its modern geographic settings to the changes of large-scale circulations.

Given the previous limitations, the interpretation of the simulation results should not focus on the absolute value of a certain quantity but the differences between PLIO and PD simulations. In our simulations, QB has a higher ΔS in PLIO than in PD. By analyzing a WRF-downscaled, high-resolution atmospheric data set, Scherer (2020) found that the mean annual ΔS in the QB from 2000–2014 is close to zero. Jiao et al. (2015) investigated the terrestrial water storage in the QB using data from the Gravity Recovery and Climate Experiment over the period from 2003–2012 and found an increase in groundwater. Since the present-day ΔS in the QB is non-negative, the higher ΔS simulated in PLIO indicates that the ΔS could have been positive under the mid-Pliocene climate, so the mega-lake system could have maintained stability and survived the continuous aridification process in the area. The same explanation of the survival of the Qaidam mega-lake system in the mid-Pliocene was offered by Scherer (2020), who found physically-based evidence that mean annual ΔS in the QB is driven by $Q2$ and the impact of $T2$ is small and not significant. Our results support these findings, since the higher annual ΔS in PLIO is consistent with the higher $Q2$, even though PLIO shows a lower $T2$ (Table 2).

As mentioned before, the PLIO simulation did not include a mega-lake system. Therefore, the feedback mechanism of the lake extent on the ΔS was not captured. Under a positive ΔS, the lake will grow and finally reach a maximum size, at which the lake area cannot increase further due to the decrease in ΔS caused by increased evaporation. The size limit that the lake can grow into, is called the equilibrium lake state. Scherer (2020) applied a semi-empirical model to project the equilibrium lake state using different values for change in P and lake evaporation in the QB. According to the estimation of Scherer (2020), an increase in annual P of $50\,\mathrm{mm\,a^{-1}}$ under mean annual lake evaporation of $800\,\mathrm{mm\,a^{-1}}$ would lead to an equilibrium lake state with a lake extent of $8067\,\mathrm{km^2}$ and a rise of the lake level of 21 m. Our downscaling results depict an annual increase in P of $63\,\mathrm{mm\,a^{-1}}$ in PLIO (Table 2), which would then result in higher values of lake extent and lake level at the equilibrium lake state. Future studies could include a lake based on those estimations in the RCM to simulate the effect of lake size on regional climate in the QB.

4.2 Large-scale systems controlling the ΔS in the QB

The changes in large-scale circulation patterns in PLIO are in good agreement with recent modeling studies (Zhang et al., 2013; Li et al., 2015; Huang et al., 2019). The results of these studies are based on simulations made by the Pliocene Model Intercomparison

Project (PlioMIP) using PRISM3D as boundary conditions, which is the same as our forcing ECHAM5 simulation for the mid-Pliocene. Li et al. (2015) found a global poleward shift of the mid-latitude westerlies and an increase of the zonal wind on the poleward flank of the westerly jet in the mid-Pliocene. The poleward shift of the mid-latitude westerlies is accompanied by a poleward shift of Hadley and Ferrel cells. The intensification and northwestward extension of the EASM in the mid-Pliocene are also simulated by models in PlioMIP (Zhang et al., 2013; Huang et al., 2019). Huang et al. (2019) compared the modeled results to paleontological data from 43 sites throughout China. The northern margin of the EASM indicated by the wet-dry boundary located further northwest in the mid-Pliocene (Figure 4 in Huang et al., 2019), which is roughly consistent with their modeled results.

There exists a debate on which large-scale system dominates the hydroclimate in the QB in previous studies based on proxy reconstructions. Caves et al. (2015) summarized published data of the spatial distribution of oxygen isotopes in precipitation over High Mountain Asia since the early Eocene (∼56 Ma BP). They found that sites at the QB show consistently higher δO_{18} values in the paleo-precipitation compared to sites in the southern TP, which indicates that westerlies have dominated the moisture supply over the QB since the early Eocene. The authors concluded that the reduction in moisture supply by the westerlies since the early Eocene, rather than uplift of the TP or changes in ISM strength, is the driver of the step-wise drying in central Asia. The modern EASM is believed to have a weak or no influence on the QB (e.g. Yu & Lai, 2012; Huang et al., 2019). This is also shown in our PD simulation. There is no westward moisture transport across the eastern border of the Qaidam box in the course of the year (Figure 6b). Xu et al. (2011) found a significant correlation between the tree ring δO_{18} series collected from the eastern margin of the QB and the strength of EASM from 1873 to 1975. Y. Miao et al. (2011) examined a pollen record from the KC-1 core, which was extracted in the western part of the QB and covers a period of 18 Ma to 5 Ma. A transition from a warm-wet climate to a cold-dry climate was found in the QB during this period and the authors concluded that this transition was driven by the evolution of the East Asia Monsoon system. Our moisture budget analysis shows that the mid-latitude westerlies dominate the AWT over the QB in both PLIO and PD (Table 3). However, the difference of the moisture budget in the QB between PLIO and PD is a combined effect of changes in the mid-latitude westerlies and the EASM.

4.3 Implications for the future

The mid-Pliocene warm period is considered as an analog of the future anthropogenic warming since both time periods feature a higher CO2 concentration compared to the modern level (Burke et al., 2018). Previous studies reveal that both the mid-Pliocene and projected future climates show similar large-scale atmospheric circulations to some extend. For example, Y. Sun et al. (2013) applied three Atmosphere-Ocean General Circulation Model simulations for Representative Concentration Pathway (RCP) 4.5 scenario, mid-Pliocene, and present-day. Their results showed a poleward expansion and an intensification of the Hadley cell over the subtropics under both mid-Pliocene and future climates, but the response of the Walker cell depicts some discrepancies. A conclusion was drawn that the Hadley cell in the mid-Pliocene can be a good analog of the Hadley cell in the future due to the linear relationship between the south-north thermal contrast and the CO2 concentration. But this analog hypothesis has limitations since the response of the east-west thermal contrast to CO2 concentration is more complicated and not similar. The monsoon dynamics between the mid-Pliocene climate and the projected future climate under the Extended Concentration Pathway version 4.5, which is an extension of RCP4.5 beyond 2100, were also investigated in a prior study (Y. Sun et al., 2018), who found that both climates show large-scale similarities and an enhanced EASM, which is due to the increase in thermally controlled large-scale moisture transport.

Combined with our results and discussions, the high similarity of large-scale circulations between the mid-Pliocene climate and the projected future climate implies that ΔS in the QB could increase in the future when the EASM extends into the QB and AWT by the westerlies increases. An increased ΔS would lead to the recharge of groundwater reservoirs and subsequent rise of lake levels in the QB.

5 Conclusions

In this study, we utilized the WRF model for dynamical downscaling of ECHAM5 global simulations for the present day and the mid-Pliocene. The downscaling results show that the annual ΔS in the QB in PLIO is higher than that in PD. Significantly higher ΔS in the QB in PLIO is suggested for winter, spring, and autumn. In summer, the difference in ΔS between PLIO and PD is not significant. The positive annual difference in ΔS between PLIO and PD indicates that, since ΔS under present conditions is non-negative, ΔS in the QB could have been positive during the mid-Pliocene. As a consequence, the mega-lake system could have survived the continuous aridification throughout the Pliocene.

The annual moisture budget in the QB is higher in PLIO, corresponding with the higher ΔS in PLIO. Higher moisture input from the western border and lower moisture output at the eastern border are the main reason for the higher annual moisture budget and higher ΔS in PLIO. These two borders are both under the influence of mid-latitude westerlies. The eastern border is additionally regulated by the EASM in PLIO. In PLIO, the mid-latitude westerlies contract poleward and intensify over the QB in winter, spring, and autumn, transporting more moisture into the QB through its western border. In summer, the strengthening of the EASM accompanied by weakened westerlies in PLIO leads to the decrease of moisture output at the eastern border.

We conclude that the strengthening of the mid-latitude westerlies in all seasons, except for summer, and the intensification of the EASM lead to higher moisture budget and thus, higher ΔS in the QB under the mid-Pliocene climate. The mid-Pliocene climate shares similarities in large-scale circulations with projected future climate scenarios. Thus, our results can contribute to a better understanding of the impacts of climate change and future lake development in central Asia.

Data Availability Statement

The WRF V4.1.2 model used in this study is freely available under the official github depository of WRF: https://github.com/wrf-model/WRF/releases. The setup files for running the WRF model, i.e., *namelist.wps* and *namelist.input*, are included in the supplementary material.

Acknowledgments
This work was supported by the German Federal Ministry of Education and Research (BMBF) programm Central Asia - Monsoon Dynamics and Geo-Ecosystems II (CAME II) within Q-TiP project Quaternary Tipping Points of Lake Systems in the Arid Zone of Central Asia (code 03G08063C and 03G08063A to D.S. and to T.A.E, respectively). The authors thank Tom Grassmann for his administrative work on the high-performance computing cluster.

References

Berg, L. K., Gustafson, W. I., Kassianov, E. I., & Deng, L. (2012). Evaluation of a Modified Scheme for Shallow Convection: Implementation of CuP and Case Studies. *Monthly Weather Review*, *141*(1), 134–147. doi: 10.1175/mwr-d-12-00136.1

Botsyun, S., Ehlers, T., Mutz, S., Methner, K., Krsnik, E., & Mulch, A. (2020, jan). Opportunities and challenges for paleoaltimetry in small orogens: Insights from the European Alps. *Geophys. Res. Lett.*. Retrieved from https://onlinelibrary.wiley.com/doi/abs/10.1029/2019GL086046 doi: 10.1029/2019GL086046

Brubaker, K. L., Entekhabi, D., & Eagleson, P. (1993). Estimation of continental precipitation recycling. *Journal of Climate*, *6*(6), 1077–1089.

Burke, K. D., Williams, J. W., Chandler, M. A., Haywood, A. M., Lunt, D. J., & Otto-Bliesner, B. L. (2018). Pliocene and Eocene provide best analogs for near-future climates. *Proc. Natl. Acad. Sci. U. S. A.*, *115*(52), 13288–13293. doi: 10.1073/pnas.1809600115

Caves, J. K., Winnick, M. J., Graham, S. A., Sjostrom, D. J., Mulch, A., & Chamberlain, C. P. (2015). Role of the westerlies in central asia climate over the cenozoic. *Earth and Planetary Science Letters*, *428*, 33–43.

Copernicus Climate Change Service (C3S). (2017). *ERA5: Fifth generation of ECMWF atmospheric reanalyses of the global climate . Copernicus Climate Change Service Climate Data Store (CDS), date of access: November 04, 2019. https://cds.climate.copernicus.eu/cdsapp#!/home.*

Curio, J., Maussion, F., & Scherer, D. (2015, mar). A 12-year high-resolution climatology of atmospheric water transport over the Tibetan Plateau. *Earth Syst. Dyn.*, *6*(1), 109–124. Retrieved from https://www.earth-syst-dynam.net/6/109/2015/ doi: 10.5194/esd-6-109-2015

Dowsett, H., Dolan, A., Rowley, D., Moucha, R., Forte, A. M., Mitrovica, J. X., ... others (2016). The prism4 (mid-piacenzian) paleoenvironmental reconstruction. *Climate of the Past*, *12*(7), 1519–1538.

Dowsett, H., Robinson, M., Haywood, A., Salzmann, U., Hill, D., Sohl, L., ... Stoll, D. (2010). The prism3d paleoenvironmental reconstruction. *Stratigraphy*, *7*(2-3), 123–139.

Dowsett, H., Thompson, R., Barron, J., Cronin, T., Fleming, F., Ishman, S., ... Holtz Jr, T. (1994). Joint investigations of the middle pliocene climate i: Prism paleoenvironmental reconstructions. *Global and Planetary Change*, *9*(3-4), 169–195.

Dudhia, J. (1989). Numerical study of convection observed during the winter monsoon experiment using a mesoscale two-dimensional model. *Journal of the atmospheric sciences*, *46*(20), 3077–3107.

Feng, L., & Zhou, T. (2012). Water vapor transport for summer precipitation over the tibetan plateau: Multidata set analysis. *Journal of Geophysical Research: Atmospheres*, *117*(D20).

Hong, S.-Y., Noh, Y., & Dudhia, J. (2006). A new vertical diffusion package with an explicit treatment of entrainment processes. *Monthly weather review*, *134*(9), 2318–2341.

Huang, X., Jiang, D., Dong, X., Yang, S., Su, B., Li, X., ... Wang, Y. (2019). Northward migration of the northern edge of the east asian summer monsoon during the mid-pliocene warm period: Simulations and reconstructions. *Journal of Geophysical Research: Atmospheres*, *124*(3), 1392–1404.

Jiao, J. J., Zhang, X., Liu, Y., & Kuang, X. (2015, oct). Increased Water Storage in the Qaidam Basin, the North Tibet Plateau from GRACE Gravity Data. *PLoS One*, *10*(10), e0141442. Retrieved from https://dx.plos.org/10.1371/journal.pone.0141442 doi: 10.1371/journal.pone.0141442

Jiménez, P. A., Dudhia, J., González-Rouco, J. F., Navarro, J., Montávez, J. P., & García-Bustamante, E. (2012). A revised scheme for the wrf surface layer formulation. *Monthly Weather Review*, *140*(3), 898–918.

Kezao, C., & Bowler, J. M. (1986, may). Late pleistocene evolution of salt lakes in the Qaidam basin, Qinghai province, China. *Palaeogeogr. Palaeoclimatol. Palaeoecol.*, *54*(1-4), 87–104. Retrieved from https://linkinghub.elsevier.com/retrieve/pii/0031018286901197 doi: 10.1016/0031-0182(86)90119-7

Koffi, E., Graham, E., & Mätzler, C. (2013). The water vapour flux above switzerland and its role in the august 2005 extreme precipitation and flooding. *Meteorologische*

Zeitschrift, *22*(3), 328–341.

Lehner, B., & Grill, G. (2013). Global river hydrography and network routing: baseline data and new approaches to study the world's large river systems. *Hydrological Processes*, *27*(15), 2171–2186.

Li, X., Jiang, D., Zhang, Z., Zhang, R., Tian, Z., & Yan, Q. (2015). Mid-pliocene westerlies from pliomip simulations. *Advances in Atmospheric Sciences*, *32*(7), 909–923.

Maussion, F., Scherer, D., Finkelnburg, R., Richters, J., Yang, W., & Yao, T. (2011). WRF simulation of a precipitation event over the Tibetan Plateau, China - An assessment using remote sensing and ground observations. *Hydrol. Earth Syst. Sci.*, *15*(6), 1795–1817. doi: 10.5194/hess-15-1795-2011

Maussion, F., Scherer, D., Mölg, T., Collier, E., Curio, J., & Finkelnburg, R. (2014). Precipitation seasonality and variability over the Tibetan Plateau as resolved by the high Asia reanalysis. *J. Clim.*, *27*(5), 1910–1927. doi: 10.1175/JCLI-D-13-00282.1

Meehl, G. A., Covey, C., Delworth, T., Latif, M., McAvaney, B., Mitchell, J. F. B., ... Taylor, K. E. (2007, sep). THE WCRP CMIP3 Multimodel Dataset: A New Era in Climate Change Research. *Bull. Am. Meteorol. Soc.*, *88*(9), 1383–1394. Retrieved from `http://journals.ametsoc.org/doi/10.1175/BAMS-88-9-1383` doi: 10.1175/BAMS-88-9-1383

Miao, Y., Fang, X., Herrmann, M., Wu, F., Zhang, Y., & Liu, D. (2011). Miocene pollen record of kc-1 core in the qaidam basin, ne tibetan plateau and implications for evolution of the east asian monsoon. *Palaeogeography, Palaeoclimatology, Palaeoecology*, *299*(1-2), 30–38.

Miao, Y. F., Fang, X. M., Wu, F. L., Cai, M. T., Song, C. H., Meng, Q. Q., & Xu, L. (2013). Late Cenozoic continuous aridification in the western Qaidam Basin: evidence from sporopollen records. *Clim. Past*, *9*(4), 1863–1877. doi: 10.5194/cp-9-1863-2013

Mischke, S., Sun, Z., Herzschuh, U., Qiao, Z., & Sun, N. (2010). An ostracod-inferred large Middle Pleistocene freshwater lake in the presently hyper-arid Qaidam Basin (NW China). *Quat. Int.*, *218*(1-2), 74–85. doi: 10.1016/j.quaint.2009.03.002

Mlawer, E. J., Taubman, S. J., Brown, P. D., Iacono, M. J., & Clough, S. A. (1997). Radiative transfer for inhomogeneous atmospheres: Rrtm, a validated correlated-k model for the longwave. *Journal of Geophysical Research: Atmospheres*, *102*(D14), 16663–16682.

Morrison, H., Thompson, G., & Tatarskii, V. (2009). Impact of cloud microphysics on the development of trailing stratiform precipitation in a simulated squall line: Comparison of one-and two-moment schemes. *Monthly weather review*, *137*(3), 991–1007.

Mutz, S. G., Ehlers, T. A., Li, J., Steger, C., Paeth, H., Werner, M., & Poulsen, C. J. (2016). Precipitation δ18o over the himalaya-tibet orogen from echam5-wiso simulations: Statistical analysis of temperature, topography and precipitation. *Journal of Geophysical Research: Atmospheres*, *121*(16), 9278–9300.

Mutz, S. G., Ehlers, T. A., Werner, M., Lohmann, G., Stepanek, C., & Li, J. (2018). Estimates of late Cenozoic climate change relevant to Earth surface processes in tectonically active orogens. *Earth Surf. Dyn.*, *6*(2), 271–301. doi: 10.5194/esurf-6-271-2018

Nakicenovic, N., Alcamo, J., Davis, G., De Vries, B., Fenhann, J., Gaffin, S., ... Dadi, Z. (1990). *Special Report on Emissions Scenarios A Special Report of Working Group III of tiie Intergovernmental Panel on Climate Change* (Tech. Rep.).

Rieser, A. B., Bojar, A.-V., Neubauer, F., Genser, J., Liu, Y., Ge, X.-H., & Friedl, G. (2009, jul). Monitoring Cenozoic climate evolution of northeastern Tibet: stable isotope constraints from the western Qaidam Basin, China. *Int. J. Earth Sci.*, *98*(5), 1063–1075. Retrieved from `http://link.springer.com/10.1007/s00531-008-0304-5` doi: 10.1007/s00531-008-0304-5

Roeckner, E., Baeuml, G., Bonaventura, L., Brokopf, R., Esch, M., Giorgetta, M., ... Tompkins, A. (2003). *The general circulation model ECHAM5. Part I: Model description* (Tech. Rep.). Retrieved from `papers3://publication/uuid/54B29E7E-A721-4C90-9A14-61E6BA163B32`

Scherer, D. (2020). Survival of the qaidam mega-lake system under mid-pliocene climates

and its restoration under future climates. *Hydrology and Earth System Sciences*, *24*(7), 3835–3850.

Sun, J., Yang, K., Guo, W., Wang, Y., He, J., & Lu, H. (2020). Why has the inner tibetan plateau become wetter since the mid-1990s? *Journal of Climate*, 1–45.

Sun, Y., Ramstein, G., Contoux, C., & Zhou, T. (2013). A comparative study of large-scale atmospheric circulation in the context of a future scenario (rcp4. 5) and past warmth (mid-pliocene). *Climate of the Past*, *9*(4).

Sun, Y., Ramstein, G., Li, L. Z., Contoux, C., Tan, N., & Zhou, T. (2018). Quantifying east asian summer monsoon dynamics in the ecp4. 5 scenario with reference to the mid-piacenzian warm period. *Geophysical Research Letters*, *45*(22), 12–523.

Taylor, K. E., Stouffer, R. J., & Meehl, G. A. (2012, apr). An Overview of CMIP5 and the Experiment Design. *Bull. Am. Meteorol. Soc.*, *93*(4), 485–498. Retrieved from `http://journals.ametsoc.org/doi/abs/10.1175/BAMS-D-11-00094.1` doi: 10.1175/BAMS-D-11-00094.1

Tewari, M., Chen, F., Wang, W., Dudhia, J., LeMone, M., Mitchell, K., ... Cuenca, R. (2004). Implementation and verification of the unified noah land surface model in the wrf model. In *20th conference on weather analysis and forecasting/16th conference on numerical weather prediction* (Vol. 1115, pp. 2165–2170).

Wang, J., Fang, X., Appel, E., & Song, C. (2012). Pliocene-Pleistocene Climate Change At the NE Tibetan Plateau Deduced From Lithofacies Variation In the Drill Core SG-1, Western Qaidam Basin, China. *J. Sediment. Res.*, *82*(12), 933–952. doi: 10.2110/jsr.2012.76

Wang, X., Tolksdorf, V., Otto, M., & Scherer, D. (2020). Wrf-based dynamical downscaling of era5 reanalysis data for high mountain asia: Towards a new version of the high asia refined analysis. *International Journal of Climatology*.

Wang, Z., Duan, A., Yang, S., & Ullah, K. (2017). Atmospheric moisture budget and its regulation on the variability of summer precipitation over the tibetan plateau. *Journal of Geophysical Research: Atmospheres*, *122*(2), 614–630.

Wilks, D. S. (2016, dec). "The Stippling Shows Statistically Significant Grid Points: How Research Results are Routinely Overstated and Overinterpreted, and What to Do about It. *Bull. Am. Meteorol. Soc.*, *97*(12), 2263–2273. Retrieved from `http://journals.ametsoc.org/doi/10.1175/BAMS-D-15-00267.1` doi: 10.1175/BAMS-D-15-00267.1

Xu, G., Chen, T., Liu, X., An, W., Wang, W., & Yun, H. (2011). Potential linkages between the moisture variability in the northeastern qaidam basin, china, since 1800 and the east asian summer monsoon as reflected by tree ring δ18o. *Journal of Geophysical Research: Atmospheres*, *116*(D9).

Yapiyev, V., Sagintayev, Z., Inglezakis, V. J., Samarkhanov, K., & Verhoef, A. (2017). Essentials of endorheic basins and lakes: A review in the context of current and future water resource management and mitigation activities in central asia. *Water*, *9*(10), 798.

Yu, L., & Lai, Z. (2012). Osl chronology and palaeoclimatic implications of aeolian sediments in the eastern qaidam basin of the northeastern qinghai-tibetan plateau. *Palaeogeography, Palaeoclimatology, Palaeoecology*, *337*, 120–129.

Zhang, R., Yan, Q., Zhang, Z. S., Jiang, D., Otto-Bliesner, B. L., Haywood, A. M., ... others (2013). Mid-pliocene east asian monsoon climate simulated in the pliomip. *Climate of the Past*, *9*, 2085–2099.

Figure 1.

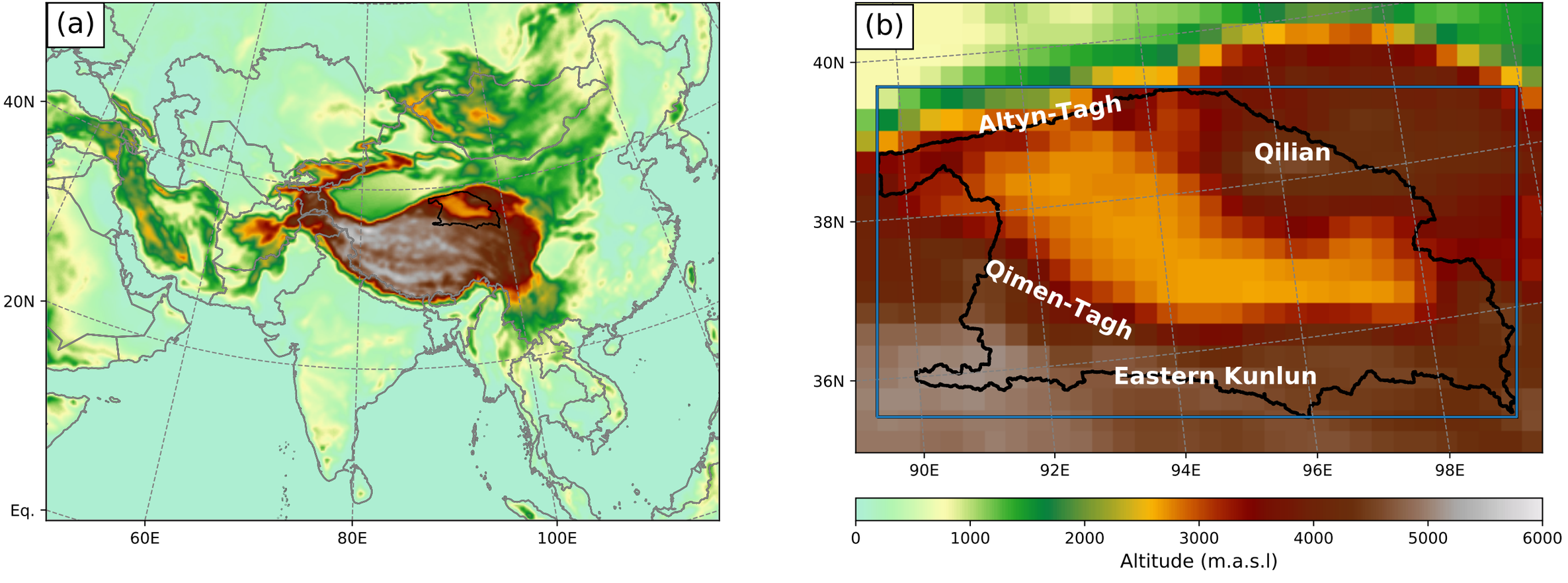
(a)
40N
20N
Eq.
60E
80E
100E
(b)
40N
38N
36N
Altyn-Tagh
Qilian
Qimen-Tagh
Eastern Kunlun
90E
92E
94E
96E
98E
0
1000
2000
3000
4000
5000
6000
Altitude (m.a.s.l)

Figure 2.

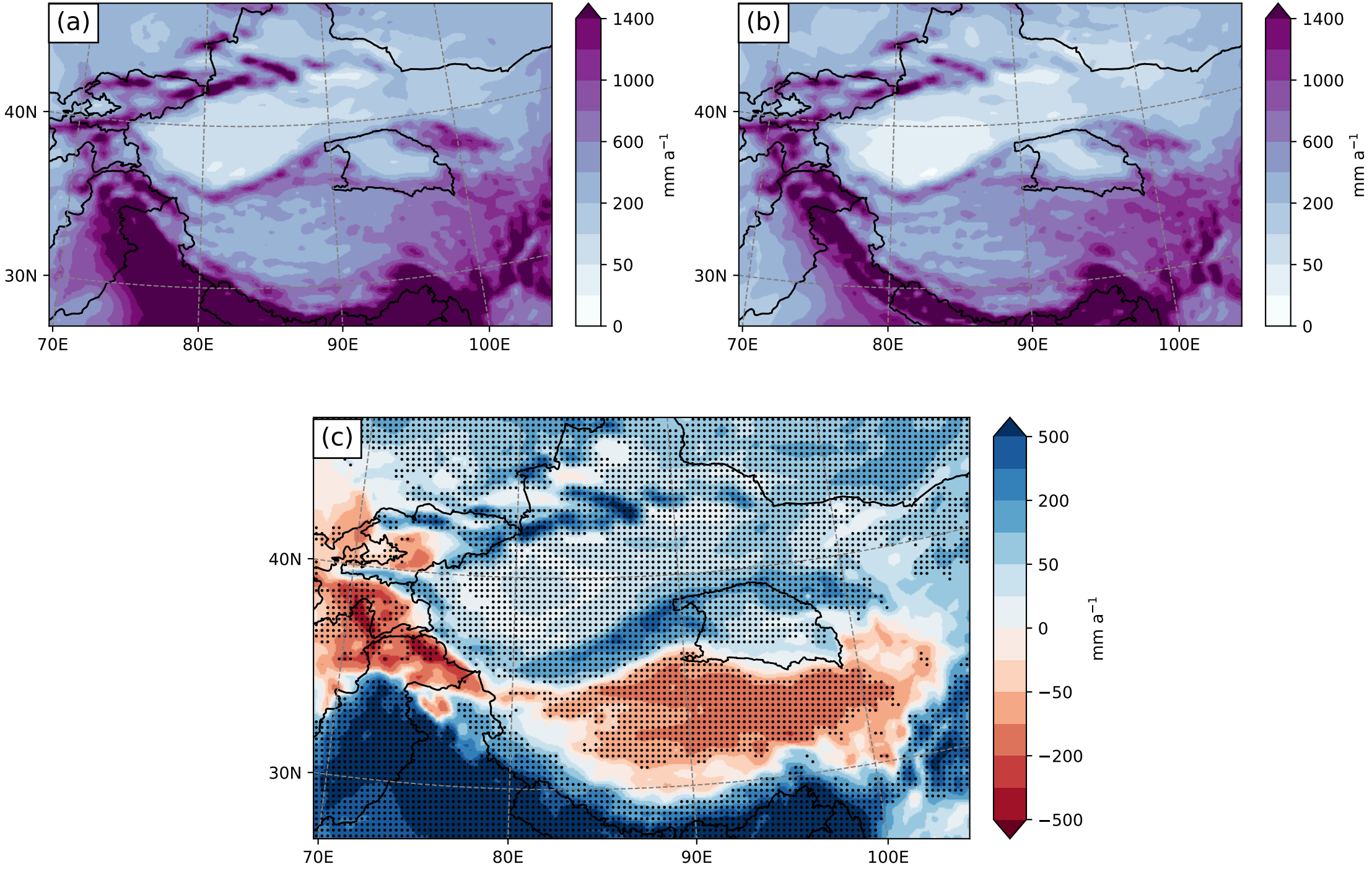
(a)
(b)
(c)
40N
30N
70E
80E
90E
100E
1400
1000
600
200
50
0
500
−50
−200
−500
mm a^{-1}

Figure 3.

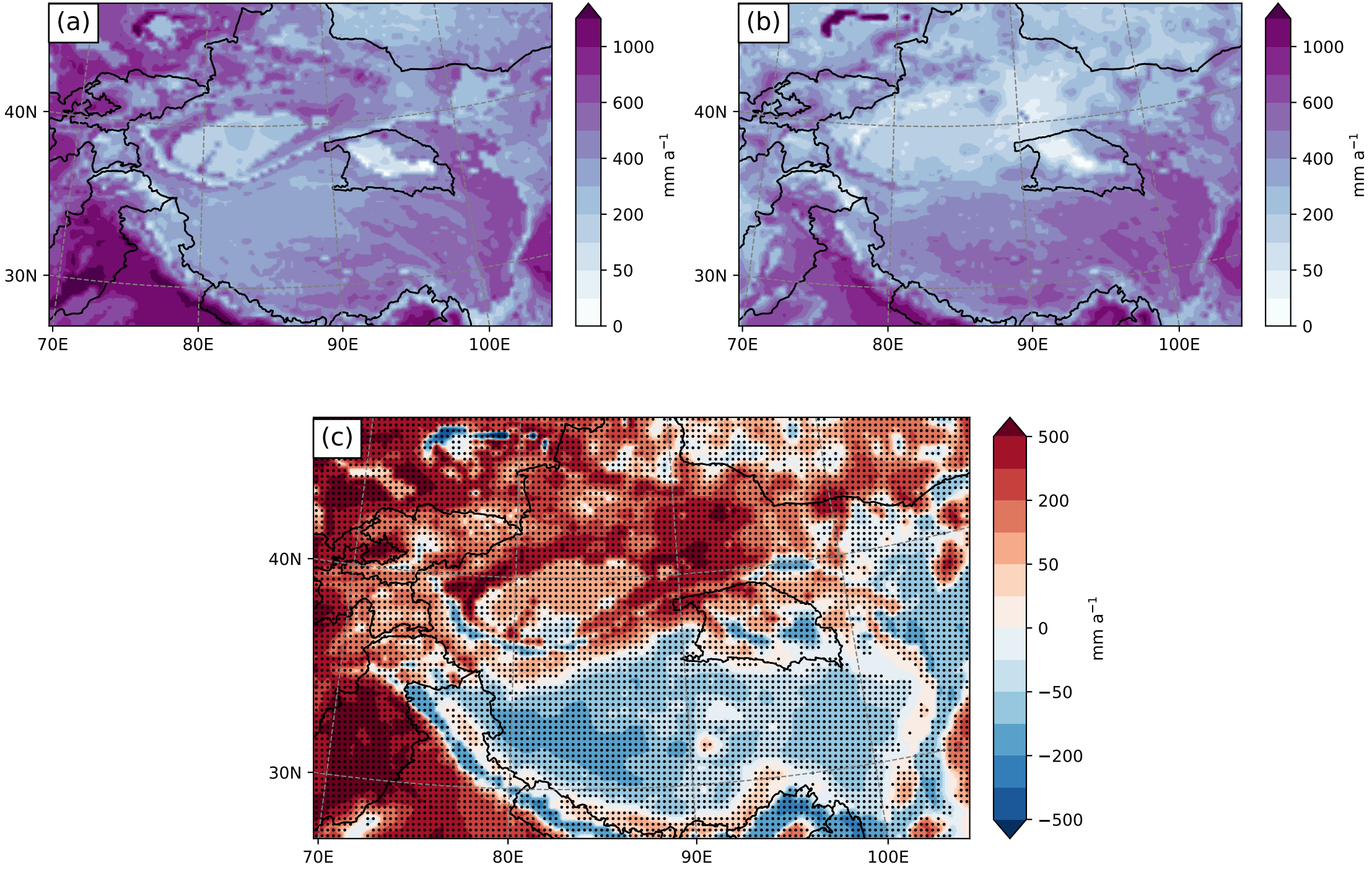
(a)
(b)
(c)
40N
30N
70E
80E
90E
100E
1000
600
400
200
50
0
500
−50
−200
−500
mm a^{-1}

Figure 4.

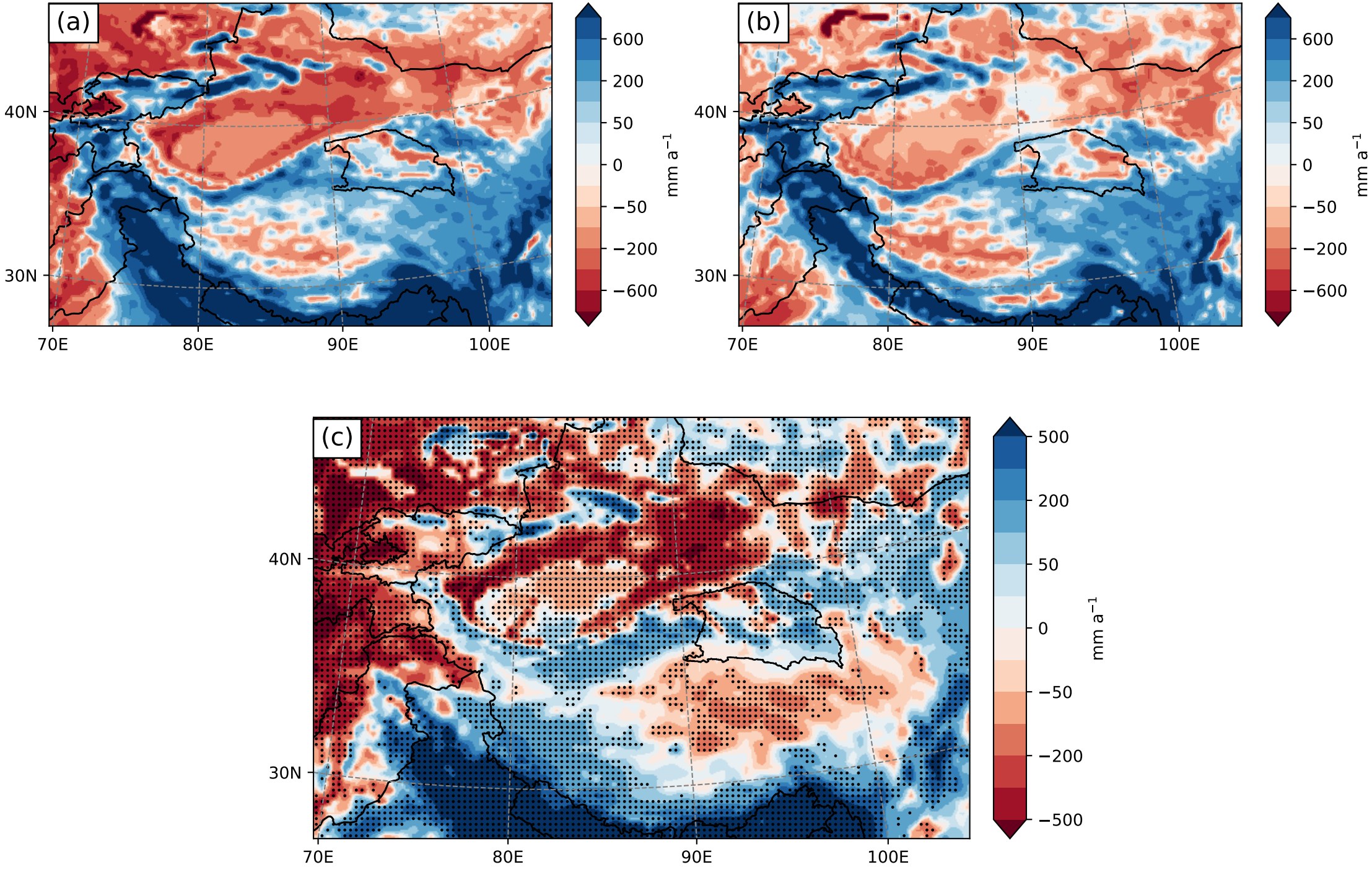
(a)
(b)
(c)
40N
30N
70E
80E
90E
100E
600
200
50
0
−50
−200
−600
500
−500
mm a^{-1}

Figure 5.

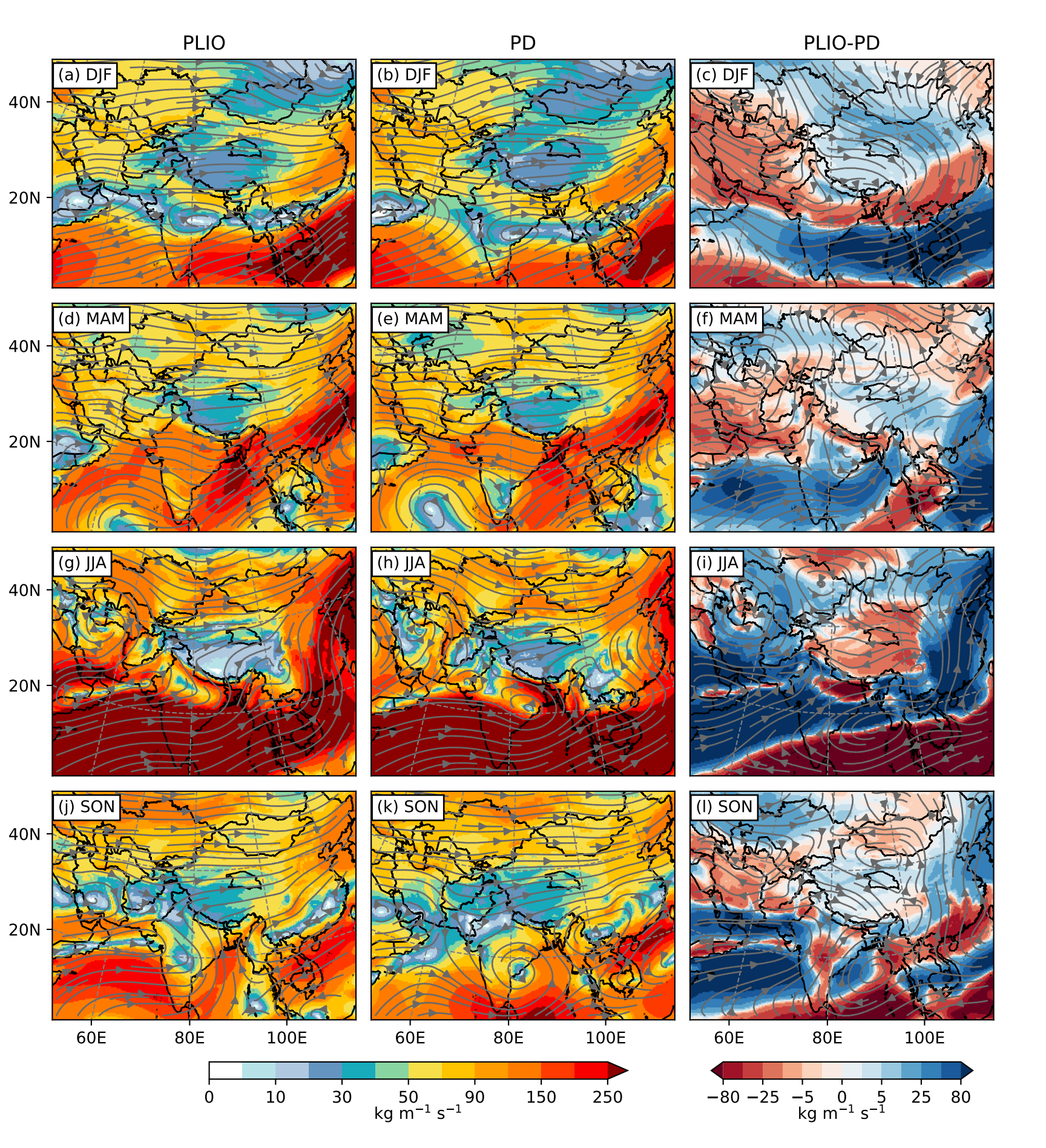
PLIO
PD
PLIO-PD
(a) DJF
(b) DJF
(c) DJF
(d) MAM
(e) MAM
(f) MAM
(g) JJA
(h) JJA
(i) JJA
(j) SON
(k) SON
(l) SON
40N
20N
60E
80E
100E
0
10
30
50
90
150
250
kg m^{-1} s^{-1}
−80
−25
−5
0
5
25
80
kg m^{-1} s^{-1}

Figure 6.

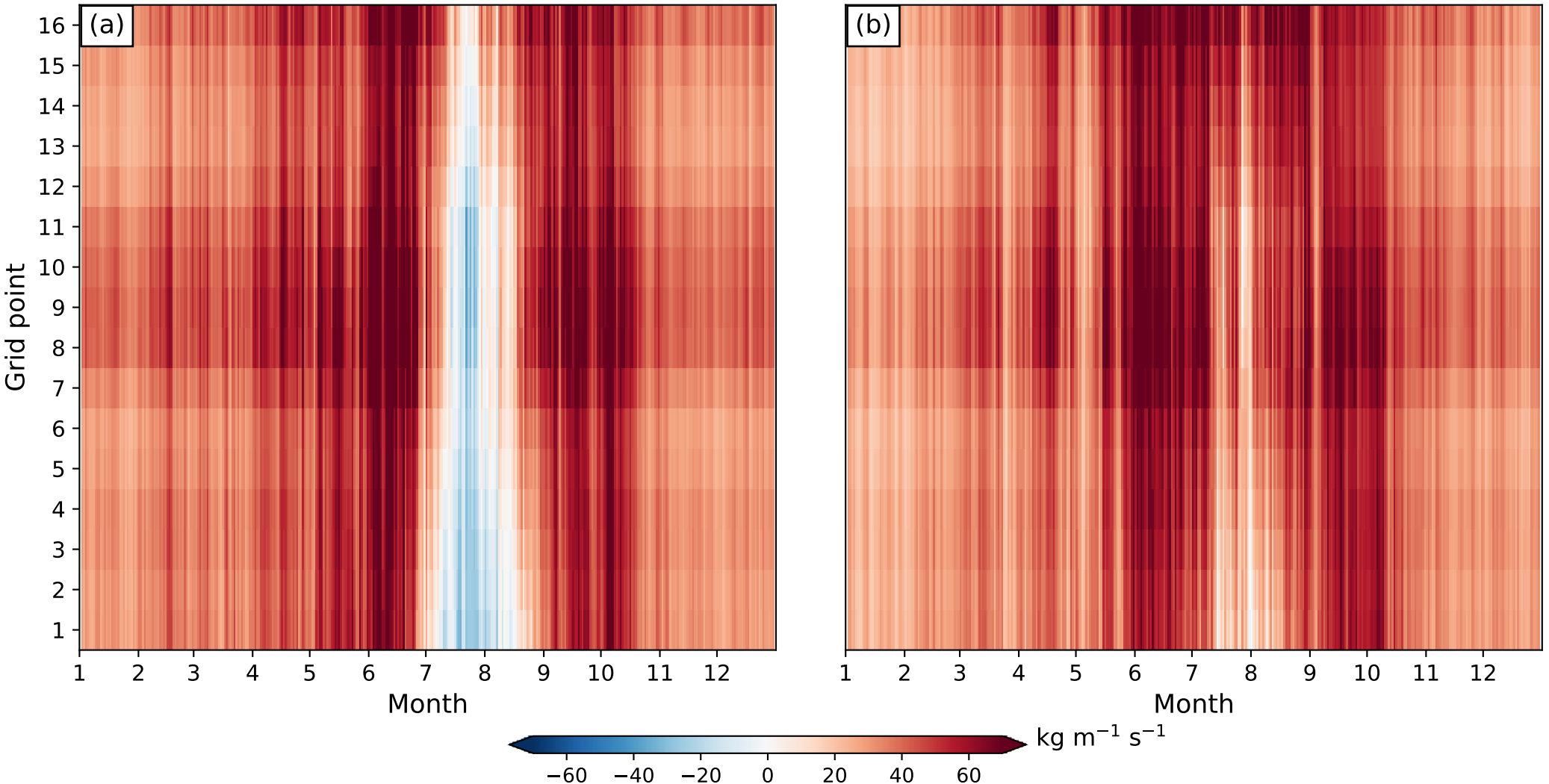
(a)
(b)
Grid point
Month
Month
kg m^{-1} s^{-1}
−60 −40 −20 0 20 40 60

Figure 7.

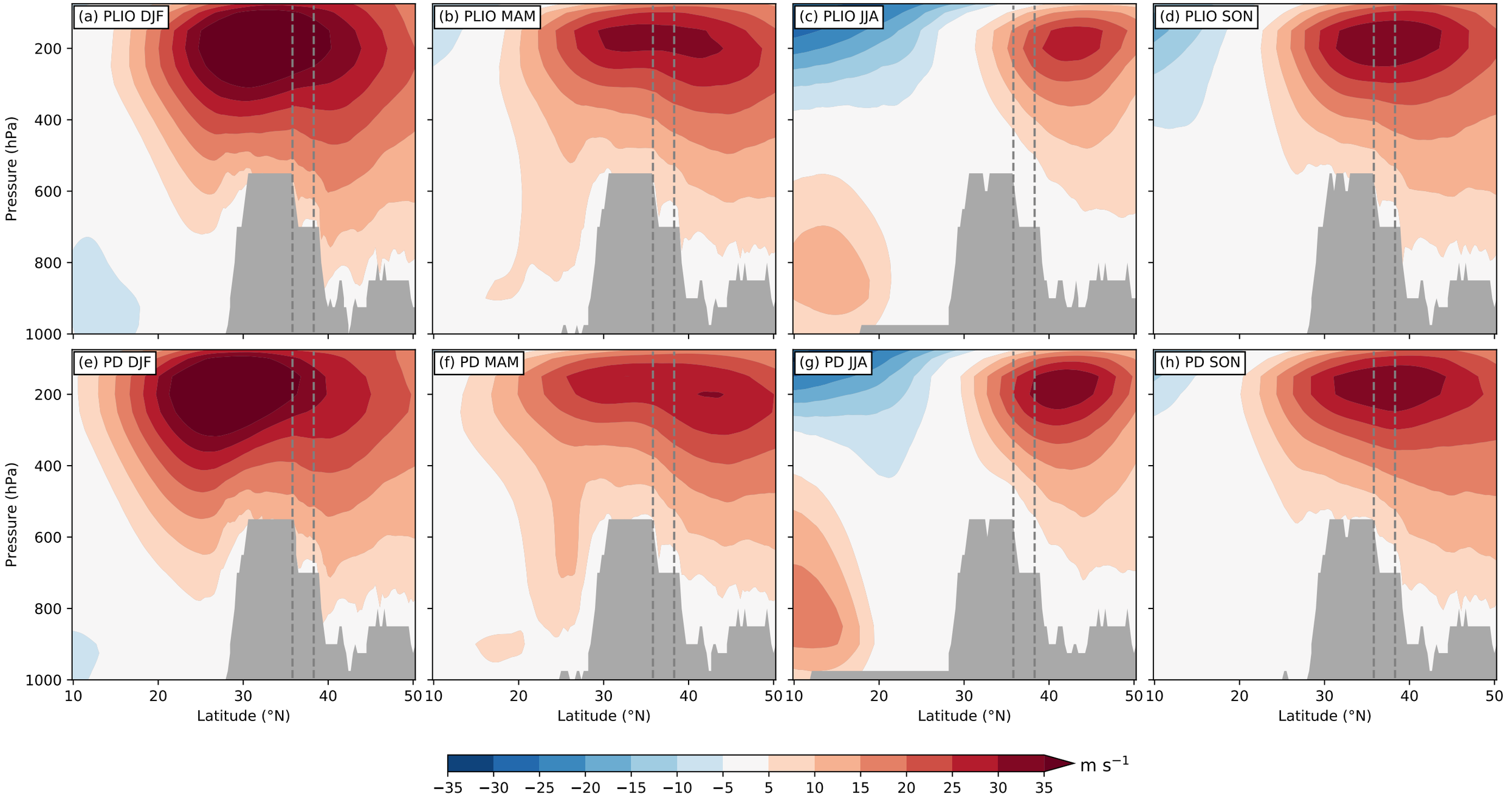
(a) PLIO DJF
(b) PLIO MAM
(c) PLIO JJA
(d) PLIO SON
(e) PD DJF
(f) PD MAM
(g) PD JJA
(h) PD SON
Pressure (hPa)
200
400
600
800
1000
10
20
30
40
50
Latitude (°N)
−35 −30 −25 −20 −15 −10 −5 5 10 15 20 25 30 35
m s^{-1}

Figure 8.

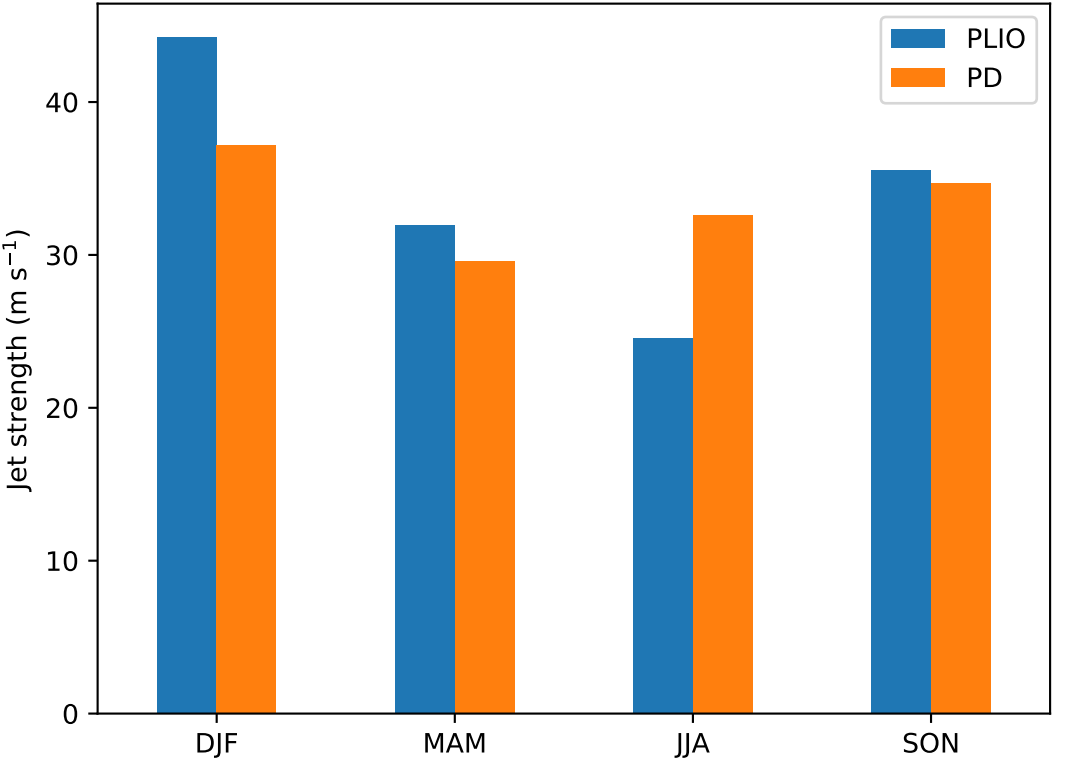
PLIO
PD
Jet strength (m s^{-1})
0
10
20
30
40
DJF
MAM
JJA
SON

Figure 9.

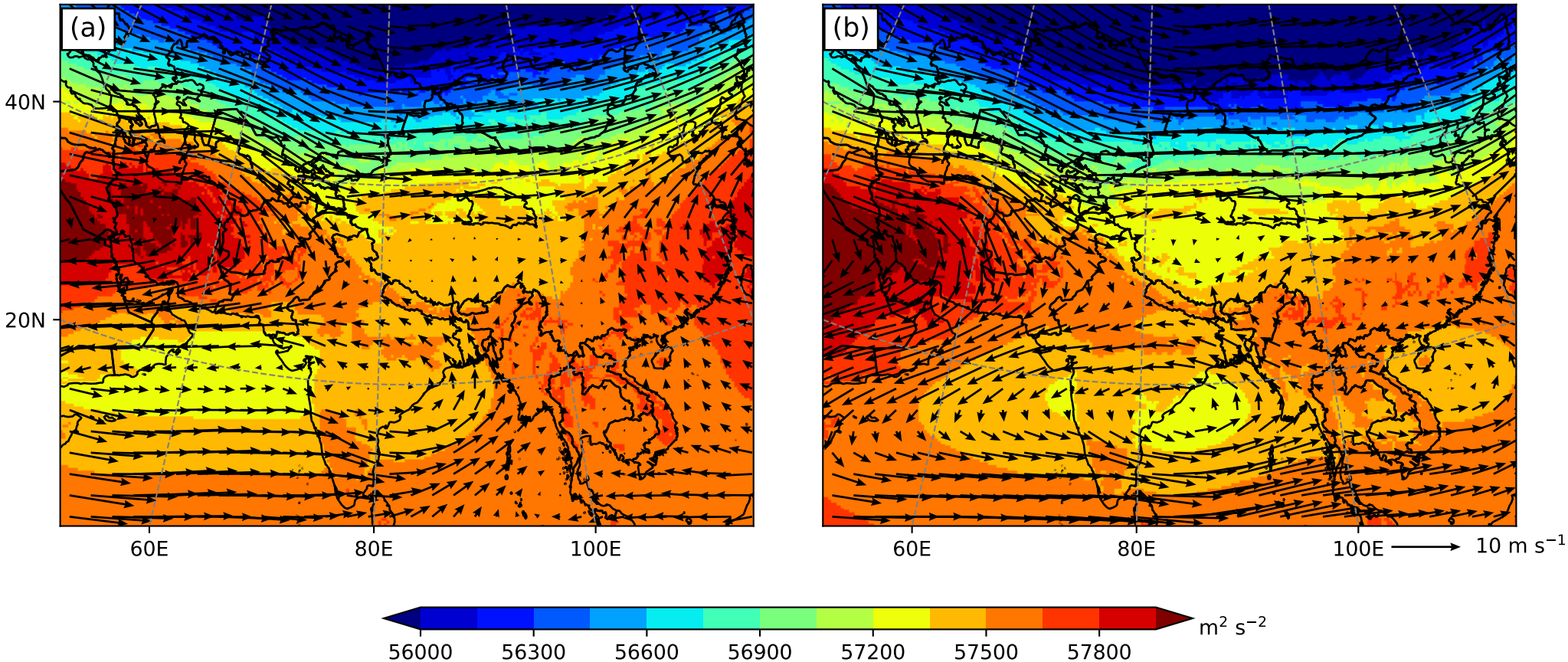
(a)
(b)
40N
20N
60E
80E
100E
60E
80E
100E
10 m s^{-1}
56000
56300
56600
56900
57200
57500
57800
m^2 s^{-2}

Figure 10.

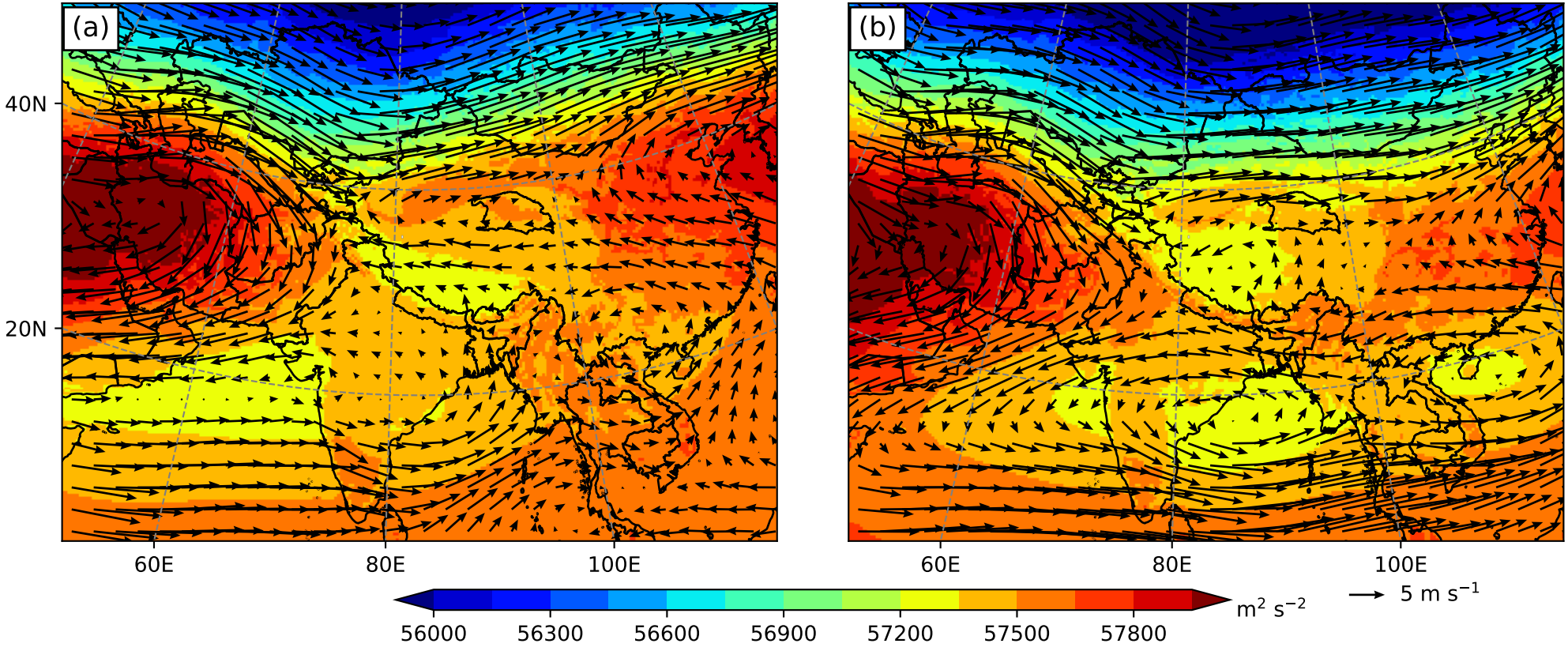
(a)
(b)
40N
20N
60E
80E
100E
60E
80E
100E
56000
56300
56600
56900
57200
57500
57800
m² s⁻²
5 m s⁻¹